Revision 2 Thorite: An Oddity in Phase Stability Amongst the Zircon-Structured Orthosilicates at High Pressures

Andrew C. Strzelecki[1,2,3], Jason L. Baker[3], Stella Chariton[4], Xiaodong Zhao[1], Vitali Prakapenka[4], David Bollinger[2], Sohan Ahmed[1], Jeffrey Fortner[5], Stephanie Szenknect[6], Adel Mesbah[7], John S. McCloy[1,2], Choong-Shik Yoo[1,2], Rodney C. Ewing[8], Nicolas Dacheux[6], Hongwu Xu[3,9], Xiaofeng Guo[1,2*]

[1] *Department of Chemistry, Washington State University, Pullman, WA 99164, United States*

[2] *School of Mechanical and Materials Engineering, Washington State University, Pullman, WA 99164, United States*

[3] *Earth and Environmental Sciences Division, Los Alamos National Laboratory, Los Alamos, NM, 87545, United States*

[4] *Center for Advanced Radiation Sources, University of Chicago, Chicago, IL 60439, USA*

[5] *Nuclear Energy and Fuel Cycle Division, Oak Ridge National Laboratory, Oak Ridge, TN 37830, United States*

[6] *ICSM, Univ Montpellier, CNRS, CEA, ENSCM, Site de Marcoule, Bagnols sur Cèze, 30207, France*

[7] *Univ Lyon, Université Lyon 1, Institut de Recherches sur la Catalyse et l'Environnement de Lyon, IRCELYON, UMR5256, CNRS, Villeurbanne, France*

[8] *Department of Earth and Planetary Sciences, Stanford University, Stanford, California 94305, United States*

[9] *School of Molecular Sciences and Center for Materials of the Universe, Arizona State University, Tempe AZ 85287, United States*

* e-mail: x.guo@wsu.edu

Abstract:

Synthetic thorite and huttonite, two polymorphs of $ThSiO_4$, were investigated by a combination of *in situ* high-pressure synchrotron X-ray powder diffraction and *in situ* high-pressure Raman spectroscopy. The average onset pressure of the thorite-to-huttonite transition was determined to be 6.6 ± 0.2 GPa, using both techniques. The bulk moduli of thorite and huttonite were determined to be 139(9) and 246(11) GPa, respectively, by fitting their unit-cell volume data to a second order Birch-Murnaghan equation of state (EOS). Based on its bulk modulus, thorite is the most compressible zircon-structured orthosilicate, as it has the largest unit cell volume among tetravalent metal orthosilicates. The pressure derivatives of the vibrational modes of thorite were found to be consistent with those previously reported for other orthosilicates (*e.g.,* zircon, hafnon, stetindite, and coffinite), while having the smallest Grüneisen parameter. A new P-T phase diagram for $ThSiO_4$ is proposed, where the boundary of the thorite → huttonite transition is: $P(T) = (7.8 \pm 0.9\ \text{GPa}) - (0.006 \pm 0.002\ \text{GPa/K})T$. Based on the new P-T phase diagram, we further estimated the enthalpy of formation of huttonite, $\Delta H_{f,ox}$, to be 0.6 ± 6.0 kJ/mol, suggesting its metastability and rare locality in nature.

Introduction:

Zircon ($ZrSiO_4$, $I4_1/amd$) and monazite ($CePO_4$, $P2_1/n$) are important as their structures host high-field strength elements, such as Zr, Hf, rare earth element (REE), Th and U (Winter 2013; Strzelecki et al. 2024). Minerals with these structures have low chemical leaching rates, high resistance to metamictization, and high thermal stability; hence, they are often used for radiometric dating based on U-Th-Pb isotopic systematics (White 2015). Interestingly, the two polymorphs of $ThSiO_4$, thorite and huttonite, are isostructural with zircon and monazite, respectively. Thorite forms a complete solid solution with the isostructural uranium orthosilicate mineral, coffinite ($USiO_4$), which includes uranothorite phases ($Th_{1-x}U_xSiO_4$) (Guo et al. 2016; Marcial et al. 2021). In contrast, huttonite, the high temperature polymorph, possesses a monazite-type structure. Even though thorite and uranothorite are common accessory minerals, huttonite is much rarer (Pabst and Hutton 1951; Frondel 1958). The structural relation between thorite and huttonite are discussed in detail by Taylor and Ewing (1978).

The abundance of thorite and uranothorite in high P-T environments and the rarity of huttonite has always been a puzzle. While other tetravalent metal orthosilicates, such as zircon, hafnon, coffinite, and stetindite are known to exhibit a pressure-induced phase transition to the reidite structure ($I4_1/a$) (Reid and Ringwood 1969; Hazen and Finger 1979; Knittle and Williams 1993; Farnan et al. 2003; Gucsik et al. 2004; Ono et al. 2004a, 2004b; Tange and Takahashi 2004; Manoun et al. 2006; Luo and Ahuja 2008; Bose et al. 2009; Zhang et al. 2009a; Bauer et al. 2014; Stangarone et al. 2019; Strzelecki et al. 2023; Zhao et al. 2024), there has been no similar transition reported for thorite. The phase stability of thorite has only been investigated experimentally under elevated temperature and ambient pressure conditions (Taylor and Ewing 1978; Mazeina et al. 2005; Navrotsky et al. 2013). At high temperature, thorite undergoes a phase transformation to huttonite at 1483 K (Finch et al. 1964; Seydoux and Montel 1997; Mazeina et al. 2005). This likely indicates that pressure is stabilizing thorite and inhibiting its conversion to huttonite. The only insight of $ThSiO_4$ under elevated pressure conditions comes from a force-field computation study (Bose et al. 2009) and a more recent comprehensive density functional theory (DFT) study (Mondal et al. 2020). The results of the force-field computational study suggest that the thorite $\rightarrow$ huttonite transition is at around 1 GPa, followed by a huttonite $\rightarrow$ reidite transition at approximately 3 GPa (Bose et al. 2009). The more recent DFT study predicted that thorite only

undergoes the conventional thorite → reidite phase transition at 8.52 GPa, with no mention of the huttonite transition (Mondal et al. 2020).

Therefore, the objective of this study was to experimentally determine the structures and phase stabilities of thorite and huttonite under high pressure conditions through *in situ* high-pressure synchrotron X-ray diffraction (XRD) and *in situ* high-pressure Raman spectroscopy. We found through *in situ* high-pressure XRD that the thorite polymorph is not stable above 12.5 ± 0.5 GPa, in excellent agreement with 12.7 ± 0.6 GPa determined by *in situ* high-pressure Raman spectroscopy. Using these determinations, a new P-T phase diagram for $ThSiO_4$ is proposed where the boundary at the thorite-to-huttonite transition is described as: $P(T) = (7.8 \pm 0.9\ \text{GPa}) - (0.006 \pm 0.002\ \text{GPa/K})T$, suggesting that the onset pressure of the transition at 300 K is 6.0 ± 1.1 GPa.

Experimental Methods:

Sample synthesis and characterization:

Two separate batches of thorite were synthesized using the hydrothermal method. The first batch was studied by high-pressure powder synchrotron XRD and Raman spectroscopy, where a 4:1 (by volume) methanol to ethanol mixture was used as the pressure transmitting medium (PTM). The sample was prepared according to the protocol of Mesbah *et al.* (2015) through modification of a previous procedure (Hoekstra and Fuchs 1956; Fuchs and Hoekstra 1959). The reagents were Na_2SiO_3, NaOH, and $NaHCO_3$. The thorium source was prepared by dissolving thorium nitrate pentahydrate in 6 mol/L HCl and performing several cycles of evaporation and dissolution in 4 mol/L HCl to remove all traces of nitrate ions in the solution (Dacheux et al. 1996). The final thorium concentration solution was determined by inductively coupled plasma atomic emission spectroscopy (ICP-AES). The synthesis was performed under air. It consisted of first dissolving Na_2SiO_3 (0.81 g, 6.66 mmol) in water and then slowly adding the corresponding thorium amounts, always keeping a silicate excess of 10 mol % to ensure the complete complexation of the actinides. The pH of the mixture was adjusted to 11.3 ± 0.1 by dropwise adding 8 mol/L NaOH. The solutions were then buffered to pH = 8.7 ± 0.1 through the addition of $NaHCO_3$. The resulting white gelatinous mixtures were then transferred into a 23 mL Teflon lined Parr autoclaves and placed into an oven at 250 °C for 7 days. The final products were separated by centrifugation and washed twice with deionized water and once with ethanol. The solids were then dried overnight in air at room temperature.

The sample was characterized in a previous work through non-destructive means using Fourier transform infrared (FTIR) and Raman spectroscopy, and laboratory based XRD (Guo et al. 2016). The FTIR and Raman spectroscopic results confirmed the successful formation of a pure single phased thorite, which was further confirmed by XRD (Guo et al. 2016). The chemical composition of each phase was determined by electron probe microanalysis (EPMA) (Guo et al. 2016). The EPMA results indicate that the thorite sample has an ideal chemical composition of $ThSiO_4$ (Guo et al. 2016). It has been shown by Guo et al. (2015) and Strzelecki et al. (2020, 2021) that the presence of water can have profound effects on the structural and thermodynamic responses of zircon-type phases prepared *via* hydrothermal methods. For this reason, a small fraction of the samples was further characterized by thermogravimetric analysis coupled with differential scanning calorimetry (TG-DSC) to elucidate the nature of any associated water. It was clear from both the TG-DSC and FTIR results that all water molecules associated with the starting thorite was physically adsorbed water rather than structural water. A more detailed description of the synthesis can be found in Guo et al. (2016).

The second batch of thorite, which was compressed using anhydrous NaCl as the PTM, and the huttonite were synthesized by following a procedure reported by Estevenon et al. (2018). High-pressure powder synchrotron XRD was done using anhydrous NaCl as the PTM. The reagents used for synthesis were Na_2SiO_3, NaOH, $NaHCO_3$, $Th(NO_3)_4{\cdot}4H_2O$, and HNO_3. The precursor solution contained 42 mmol/L Th in the presence of 3 mol.% excess Si and 420 mmol/L of CO_3^{2-}. The final pH of the solution was adjusted to 8.6 ± 0.1 by dropwise addition of 4 mol/L NaOH. The solution was allowed to react at 250 °C for 24 hours before being washed 6 times with 18.2 MΩ-cm deionized water centrifuged at 4000 rpm for 10 mins. The resulting powder was allowed to dry at 150 °C for 2 hours and then sintered at 1000 °C, under air, for 24 hours, producing crystalline thorite. For huttonite synthesis, the concentration of the thorium solution reached 42 mmol/L. The reacting medium contained a silicate of 3 mol.% excess and CO_3^{2-} concentration equal to 420 mmol/L. The final pH of the solution was adjusted to 12.0 ± 0.1 by dropwise addition of 4 mol/L NaOH. The solution was allowed to react at 250 °C for 43 hours before being washed 5 times with 18.2 MΩ-cm deionized water centrifuged at 4000 rpm for 15 mins. The resulting powder was allowed to dry at 90° C overnight. The dry powder was then hand pressed into a pellet form and fired at 1300 °C in air, for 10 hours, yielding crystalline huttonite.

XRD analysis revealed that the thorite powdered sample obtained by the second batch had a minor ThO_2 impurity, while the huttonite sample had minor impurities of ThO_2 and thorite. An attempt was made to purify both samples through modification of the method originally published for uranothorite (Clavier et al. 2013). The method involved placing 28.91 mg of impure thorite or 46.27 mg of impure huttonite in contact with 50 mL of 1 mol/L HNO_3 and allowed to react in a 50 mL centrifuge tube. The centrifuge tube was then placed onto a Glas-Col Rugged Rotator, in vertical orientation, and allowed to constantly mix for 72 hours at 60 rpm. This would allow for more effective dissolution of ThO_2 by constantly exposing fresh unreacted surfaces. The solids and the supernatants were then separated by decantation and the remaining solids were washed 4 times with 18.2 MΩ-cm deionized water (50 mL for each stage) and once with ethanol (25 mL), allowing centrifugation for 10 mins at 4000 rpm each time. The sample was then left at room temperature for 48 hours to allow for all the ethanol to evaporate off. The remaining powders of thorite and huttonite were hand pressed into pellets. The thorite pellet was calcined at 900 °C for 2.5 hours, while the huttonite pellet was fired at 1300 °C for 8 hours. The calcined pellets were then hand ground with an agate mortar and pestle. The resulting powder was analyzed by powder XRD. Rietveld analysis of XRD data showed that the amount of ThO_2 impurity in the thorite and huttonite did not decrease appreciably after calcination (Hubert et al. 2008), with the huttonite having lesser residual thorite phase.

In situ high-pressure synchrotron XRD:

Several sets of high-pressure powder synchrotron XRD experiments were conducted at the GeoSoilEnviroCARS (GSECARS) beamline 13-ID-D of the Advanced Photon Source (APS) at Argonne National Laboratory (ANL). The high pressures generated during the experiments were attained through application of a Princeton type symmetric diamond anvil cells (DAC). The DAC were always completely sealed with Kapton tape to create secondary containment for safe handling of radioactive samples. Ruby fluorescence was used to determine the pressure in the cell. To avoid the damage of Kapton from absorbing the online Ruby laser, a small Mylar window was used to replace the Kapton in the laser light path. The X-rays had a wavelength of 0.3344 Å (37 keV), with a beam size of ~2.5 × 2.5 μm. The beams geometric parameters were calibrated using LaB_6. The detector used was a Pilatus 1M cadmium telluride (CdTe) detector. The distance from sample to detector was fixed at 237.1 mm.

The first batch of thorite, which used a 4:1 (by volume) methanol : ethanol mixture as the PTM was loaded into a 150 μm laser-drilled hole at the center of a pre-indented, 40 μm thick steel gasket. The culet size of the diamonds was 300 μm. A ruby sphere was also loaded into the DAC to measure the pressure through the shift in its R_1 fluorescence line (Mao et al. 1986). The second batch of thorite or huttonite and a piece of Pt were loaded in between two NaCl plates. NaCl was utilized as the PTM and internal pressure marker. The pressure-volume (*P-V*) equation of state (EOS) of NaCl-B1 (*Fm*-3*m*) (Dewaele et al. 2012), was used to determine the pressures in the cell. This sample/standard/PTM assembly was loaded into an electric discharge machine (EDM) drilled hole (150 μm diameter) at the center of a pre-indented (39-47 μm thickness) Re gasket. A sapphire window (Edmund Optics), with a diameter of 6.35 ± 0.05 mm and a thickness of 0.50 ± 0.05 mm, was placed at the opening of each DAC in case of failure of the diamonds.

All collected two-dimensional images were calibrated, masked, and integrated through the use of Dioptas (Prescher and Prakapenka 2015). The obtained XRD patterns of thorite and huttonite were analyzed by the Rietveld method using the General Structure Analysis System software version II (GSAS-II) (Toby and Von Dreele 2013). The background was modelled using the Chebyshev function. The starting models for the refinements for both thorite and huttonite were the structures reported by Taylor and Ewing (1978). The Rietveld refinement procedures have been described previously (Zhang et al. 2002; Xu et al. 2017; Guo et al. 2019; Baker et al. 2020; Lü et al. 2020; Strzelecki et al. 2022b, 2022a, 2023) .

In situ high-pressure Raman spectroscopy:

Raman spectroscopic measurements were performed on the first batch of thorite using a Horiba HR Evolution Labram Raman system equipped with a 532 nm laser, and an Olympus 20× long-working distance objective lens was used to visualize the sample and focus the laser into the sample chamber. All spectra were collected in the 100-1400 cm^{-1} range. The maximum laser output was 100 mW but was attenuated before interacting with the sample. The system was equipped with an 1800 gr/mm grating which yielded an effective 0.3 cm^{-1} resolution. The collected spectra were corrected by subtracting the background and fitted using a Lorentz-type function. For *in situ* high-pressure Raman spectroscopy, a Princeton-style symmetric diamond anvil cell (DAC) with Type IIb, ultra-low fluorescence 300 μm culet diamonds (Almax) were used. The sample was loaded in a drilled hole (125 μm diameter) at the center of a pre-indented (50 μm thickness)

stainless-steel gasket. Ruby spheres were placed into the sample chamber for continuous pressure determination, before and after collecting a Raman spectrum, by the pressure shift of the R1 fluorescence line (Mao et al. 1986). The PTM used was a 4:1 methanol : ethanol mixture. Raman spectra were collected on compressing the sample from ambient to 26.4 ± 1.3 GPa. Above 15.5 ± 0.8 GPa, both the deviatoric stresses in the DAC, caused by the 4:1 ethanol methanol mixture, and the sluggish kinetics of the thorite-to-huttonite transition yielded broad Raman spectra that could not be deconvoluted using Gaussian functions.

Results:

XRD of thorite using PTM of 4:1 methanol : ethanol mixture:

Figure S1 shows a plot of the collected XRD patterns as a function of pressure. The onset of the thorite $\rightarrow$ huttonite transition was 5.1 ± 0.3 GPa, which is evident by the disappearance of the (220) peak associated with thorite. The phase transition was deemed complete at 13.2 ± 0.7 GPa when no more peak could be attributed to thorite (Figure S1). Rietveld analysis was performed on all of the patterns collected from 1.5 to 10.3 GPa, which yielded R_{wp} values ranging from 4.74% to 6.65% (Table S1). No new peaks assigned to the huttonite phase were detected until 11.2 ± 0.6 GPa, and thus only the thorite phase was included in the Rietveld analysis. Above 10.3 ± 0.5 GPa, the resulting patterns were too broad and distorted to reliably fit the huttonite structure (Figure S1). This is probably due to the loss of hydrostaticity of the 4:1 methanol : ethanol mixture at high pressure. Thus, no unit cell parameters for huttonite were derived from this set of XRD data.

XRD of thorite using PTM of NaCl:

Figure 1 plots the XRD patterns as a function of pressure. The resulting refinements for thorite (with NaCl and ThO_2 as additional phases), using NaCl as the PTM, yielded R_{wp} values ranging from 2.2% to 3.2% (Table S2). The small spot size (~6.3 μm^2) of the X-ray beam allowed for multiple positions in the sample chamber to be measured at each pressure step. However, spots with both Pt and $ThSiO_4$ were not found so the pressure in the cell was determined only using the P-V EOS of NaCl. The refined unit cell parameters of thorite are shown in Figure 2. With NaCl as the PTM, thorite was found to be stable up to 6.5 ± 0.3 GPa (Table S2). The onset of the thorite $\rightarrow$ huttonite transition was 6.9 ± 0.4 GPa. This is apparent by the appearance of a new peak, associated with the (011) diffraction maxima of huttonite, which appears at $2\theta = 4.608°$. This peak

slowly grew in intensity following the compression up 9.0 ± 0.5 GPa. The phase transition was deemed complete at 12.5 ± 0.6 GPa, as reflected by the absence of visible diffraction maxima of thorite at that pressure (Figure S4). Due to the low intensity of the (011) peak of huttonite, only NaCl and ThO_2 were included as additional phases in the Rietveld analysis along with thorite, from 6.9 to 9.0 GPa.

XRD of huttonite using PTM of NaCl:

The resulting refinements for huttonite, using NaCl as the PTM, yielded R_{wp} values ranging from 3.8% to 6.0% (Table S3). The refined unit cell parameters of huttonite are listed in Table S3 and shown in Figure 2. No additional phase transitions were observed during compression. With increasing pressure, the unit cell of huttonite contracts (Figures 2 and 3). Furthermore, unlike thorite, there were no emergence or disappearance of XRD peaks in the pressure range investigated, suggesting no phase transition.

Raman spectroscopy of $ThSiO_4$ using PTM of 4:1 methanol : ethanol mixture:

The Raman spectra of $ThSiO_4$ collected during the compression to 26.4 ± 1.3 GPa are shown in Figure 4. The vibrational peak positions for thorite under ambient pressure are listed in Table 1 alongside other zircon structure-type orthosilicates (Dawson et al. 1971; Syme et al. 1977; Hoskin and Rodgers 1996; Geisler et al. 2006; Clavier et al. 2014; Estevenon et al. 2018, 2019a, 2019b, 2020; Strzelecki et al. 2021, 2023). The onset pressure of the thorite $\rightarrow$ huttonite transition was 7.7 ± 0.4 GPa, as indicated by a shoulder emerging around 870 cm^{-1}. This shoulder is likely attributed to the ν_3 antisymmetric stretching mode of the huttonite structure (Jin and Soderholm 2015). Thorite was found to be stable up to 12.7 ± 0.6 GPa, in good agreement with results from XRD analysis. Above 15.5 ± 0.8 GPa, the vibrational bands became very broad, where the broadness was likely due to the deviatoric stress as the result of the 4:1 methanol:ethanol PTM reaching its hydrostatic limit (Klotz et al. 2009) and also partially due to lesser crystallinity of the pressure-induced phase (Bauer et al. 2014). Only the vibrational bands attributed to the thorite structure could be deconvoluted and the pressure dependency of these bands were assessed (Table 2).

Theoretically, the $I4_1/amd$ space group has seventeen Raman-active vibrational modes belonging to the D_{4h} point group (Dawson et al. 1971; Kolesov et al. 2001; Clavier et al. 2014).

Among these seventeen modes, nine ($\Gamma_{int} = 2A_{1g} + 2B_{1g} + B_{2g} + 2E_g$) (Dawson et al. 1971; Kolesov et al. 2001) can be assigned to the internal vibrations (or normal modes) of the SiO_4 tetrahedron, and the remaining eight ($\Gamma_{ext} = 2B_{1g} + 3E_g$)(Dawson et al. 1971; Kolesov et al. 2001) assigned to the external vibrations (lattice modes) (Dawson et al. 1971; Hoskin and Rodgers 1996; Kolesov et al. 2001). The vibrational modes labeled as ν_1, ν_2, ν_3, and ν_4 correspond to the internal vibrations, where ν_1 (A_{1g}) and ν_3 (B_{1g}) correspond to the symmetric and antisymmetric stretching motions, respectively, and ν_2 (A_{1g}) and ν_4 (B_{1g}) correspond to the symmetric and antisymmetric bending modes, respectively (Nasdala et al. 2003). The motion of the external modes can further be classified into rotational (B_g) and translational (E_g) modes (Dawson et al. 1971; Nasdala et al. 2003; Zhao et al. 2024). Due to the interaction of SiO_4 tetrahedra with the MO_8 dodecahedra in the structure, SiO_4 tetrahedra cannot be considered strictly independent units (Syme et al. 1977). As a result of these interactions, there are no reported spectra showing all seventeen Raman-active modes for zircon structure-type materials (Clavier et al. 2014).

Discussion:

Pressure-volume equations of states:

Figure 2 shows the pressure dependence of the unit cell volumes of thorite and huttonite from the XRD experiments and their fits to the second-order Birch-Murnaghan EOS (Birch 1978). The equation describing the second-order Birch-Murnaghan EOS is:

$$P = \frac{3K_0}{2}\left[\left(\frac{V_0}{V}\right)^{\frac{7}{3}} - \left(\frac{V_0}{V}\right)^{\frac{5}{3}}\right] \quad (1)$$

in which V_0 is the zero-pressure unit cell volume, V is the cell volume at a given pressure (P), and K_0 is the bulk modulus (Birch 1978). The fits were performed with the EosFit7 software (Gonzalez-Platas et al. 2016) which includes uncertainties of the data points to derive a weighting scheme for the fit. Uncertainties include errors from the measured pressure by ruby luminescence (Mao et al. 1986) and the derived unit parameters by Rietveld analyses. While other studies on zircon-structured orthosilicates, such as the work of Ehlers et al. (2022), used higher-ordered Birch-Murnaghan EOS to fit their experimental data, it was not used in this analysis due to the limited number of data points.

The unit cell parameters can be further fitted to the one-dimensional form of the Birch-Murnaghan EOS by replacing V with either a^3, b^3, or c^3:

$$P = \frac{3M_{a,0}}{2}\left[\left(\frac{a_0}{a}\right)^7 - \left(\frac{a_0}{a}\right)^5\right], P = \frac{3M_{b,0}}{2}\left[\left(\frac{b_0}{b}\right)^7 - \left(\frac{b_0}{b}\right)^5\right], P = \frac{3M_{c,0}}{2}\left[\left(\frac{c_0}{c}\right)^7 - \left(\frac{c_0}{c}\right)^5\right] \quad (2)$$

where a_0, b_0, and c_0 are the unit cell parameters at zero pressure and $M_{a,0}$, $M_{b,0}$, and $M_{c,0}$ are the linear moduli. The values derived for M_a, M_b, and M_c can be used to further check the previously derived K_0 in Eq. 1 and give confidence in the derived values through the following relation:

$$K_{0,lm} = 3 \times \left(\frac{1}{M_{a,0}} + \frac{1}{M_{b,0}} + \frac{1}{M_{c,0}}\right)^{-1} \quad (3)$$

Lastly, the linear compressibility (β_l) of a crystal is the relative decrease in its unit cell length l when the crystal is subjected to a unit pressure and is given by the following equation:

$$\beta_l = -\left(\frac{1}{l}\right)\left(\frac{\partial l}{\partial P}\right) = -\left(\frac{1}{l}\right)\left[\frac{1}{\frac{\partial P}{\partial l}}\right] \quad (4)$$

where l is the cell parameter a, b, or c and ($\partial P/\partial a$), ($\partial P/\partial b$), or ($\partial P/\partial c$) can be derived from the above equations.

High-pressure structure of thorite:

Two *P-V* equations of state were determined for thorite based on the data collected from the two different PTMs (4:1 methanol : ethanol and NaCl). By using the second order Birch-Murnaghan EOS (Equation 1), the fit performed on the data collected with the 4:1 methanol : ethanol mixture PTM was based on the data collected from 1.5 ± 0.1 to 10.3 ± 0.5 GPa, and yielded a V_0 of 320.7(4) Å^3 and a K_0 of 153(14) GPa (Table 3). The fit performed on the data collected with the NaCl PTM used the data collected from 3.9 ± 0.2 to 9.0 ± 0.5 GPa, and yielded a V_0 of 328.3(11) Å^3 and a K_0 of 125(11) GPa (Figure 2 and Table 3). The two derived bulk moduli, using the two different PTMs, agree well with one another, giving an averaged V_0 of 324.5(6) Å^3 and K_0 of 139(9) GPa. These values are consistent with the values of other isostructural silicates (Table 3), as there is an empirical inverse linear relationship between the V_0 and K_0 (Xu et al. 2009; Strzelecki et al. 2024). As thorite possesses the largest unit cell volume of zircon-structured orthosilicates, owing to the large ionic radius of Th^{4+} in an eight-fold coordination environment (Shannon 1976), it is expected that it would be the most compressible phase.

High-pressure structure of huttonite:

The elastic properties of huttonite can be determined by examining the pressure-dependent unit cell parameter data. Fitting the unit cell volume-pressure relation from 2.7 ± 0.1 to 21.1 ± 0.18

GPa by a second order Birch-Murnaghan EOS (Figure 2) yielded a V_0 of 296.6(3) Å^3 and a K_0 of 246(11) GPa. The unit cell parameters were also fitted to the one-dimensional form of the Birch-Murnaghan EOS using Equation 2. The unit-cell parameters at zero pressure for the huttonite are: a_0 = 6.791(13) Å, b_0 = 6.976(4) Å, and c_0 = 6.512(11) Å, and the linear moduli are: $M_{a,0}$ = 147(16) GPa, $M_{b,0}$ = 255(17) GPa, and $M_{c,0}$ = 257(42) GPa. The values derived for M_a, M_b, and M_c can be used to further check the previously derived K_0 and give confidence in the derived values using Equation 3. $K_{0,l}$ obtained from linear moduli for huttonite was 206(14) GPa, which compares reasonably well with the directly derived K_0 (Table 3).

An elastic anisotropy exists among the three crystallographic axes of huttonite (*a*-, *b*- and *c*-axes). The linear compressibility (β_l) of a crystal is the relative decrease in its unit-cell length *l* when the crystal is subjected to a unit pressure and is given by Equation 4. While all the unit cell parameters (*a*, *b*, and *c*) decrease with increasing pressure, their contraction rates are quite different. The rates of contraction are in the order $a < b < c$, though the rates of contraction along the *b*-axis and *c*-axis are very close. The zero-pressure compressibility of the *a*, *b*, and *c* axes for huttonite are $(2.26 \pm 0.25) \times 10^{-3}$ GPa^{-1}, $(1.31 \pm 0.09) \times 10^{-3}$ GPa^{-1}, and $(1.30 \pm 0.21) \times 10^{-3}$ GPa^{-1}, respectively. Therefore, for huttonite, the unit cell along the *a*-axis is 1.73 and 1.74 times more compressible than along the *b*- and *c*-axes, respectively.

Grüneisen parameters:

The Raman peak positions as a function of pressure for $ThSiO_4$ up to 15.5 ± 0.8 GPa are shown in Figure 5. In contrast to what was found for $CeSiO_4$ (Strzelecki et al. 2023), the antisymmetric deformation (ν_4) was discerned from the background (Figure 4) and thus included in Figure 5. The pressure derivatives of the peak positions (dν/dP) up to 15.5 ± 0.8 GPa were computed by linear fits and are listed in Table 2. All of the internal vibrational modes of the [SiO_4] tetrahedra show positive pressure dependence on the peak position (Figure 5). Overall, the individual vibrational mode shifts (dν/dP) of thorite are comparable to those of other isostructural orthosilicate minerals including zircon, hafnon, stetindite, and coffinite (Table 2) (Knittle and Williams 1993; Manoun et al. 2006; Bauer et al. 2014; Strzelecki et al. 2023).

Using the obtained K_0 value of thorite, in conjunction with its vibrational mode shifts, we have derived the mode Grüneisen parameters (γ_i) using the following equation:

$$\gamma_i = \left(\frac{K_0}{\nu_0}\right)\left(\frac{\mathrm{d}\nu}{\mathrm{dP}}\right) \quad (5)$$

The derived γ_i values for thorite are reported in Table 2. Both the value of vibrational mode shifts and the bulk modulus values (Table 3) are smaller than those of other zircon-structure orthosilicates and so are the γ_i. This is explained by the inverse relationship between bulk modulus and unit cell volume (Xu et al. 2009). As thorite possess the largest unit cell volume of the zircon structure orthosilicates, owing to the large ionic radii of Th^{4+} in an eight-fold coordination environment (Shannon 1976), this is consistent with the existing empirical trends (Strzelecki et al. 2024).

P-T phase diagram of $ThSiO_4$:

The pressure-temperature phase diagram of $ThSiO_4$ has been previously assessed by Dachille and Roy (1964), Seydoux and Montel (1997), and Mazeina et al. (2005) using a variety of experimental techniques (Figure 6). Dachille and Roy (1964) determined the P-T phase diagram using a Bridgman-type opposed-anvil apparatus and studied the quenched solids. The P-T phase boundary determined in Dachille and Roy (1964) can be described by $P(T) = 6.7$ GPa – (0.005 GPa/K)T, suggesting an onset pressure of 5.1 GPa for the thorite to huttonite transition (Figure 6) (Dachille and Roy 1964). Seydoux and Montel (1997) used hydrothermal synthetic techniques to determine a P-T boundary line described by $P(T) = 4.5$ GPa – (0.003 GPa/K)T, which suggests a much lower onset pressure of 3.6 GPa for the thorite to huttonite transition (Figure 6). Mazeina et al. reassessed the P-T phase diagram and proposed a phase boundary described by $P(T) = 1.8$ GPa – (0.001 GPa/K)T (Figure 6) (Mazeina et al. 2005). This reassessment was based on an improved knowledge of the temperature induced phase transition of thorite-to-huttonite using differential scanning calorimetry (Mazeina et al. 2005) and also the works of Dachille and Roy and Seydoux and Montel (Dachille and Roy 1964; Seydoux and Montel 1997).

In this study, the *P-T* phase diagram was again reassessed. The reassessment was based on the pressure that huttonite was first visible during our *in situ* high-pressure powder XRD and Raman spectroscopy experiments. Additionally, the three data points of Dachille and Roy which yielded a mixed thorite + huttonite phase were included in the reassessment (Dachille and Roy 1964) (Figure 6). Thus, the phase boundary of thorite-to-huttonite can be described by $P(T) = (7.8 \pm 0.9$ GPa) – $(0.006 \pm 0.002$ GPa/K)T, suggesting an onset pressure of the transition to be 6.0 ± 1.1 GPa. It can also be inferred from Figure 6 that the phase stability line determined here implies a temperature of transition, at ambient pressures, of thorite-to-huttonite of 1252 K. This

value agrees well with the value determined by Seydoux and Montel (1997) of 1283 K even though this value was not considered in our reassessment.

The small discrepancy, of ~30 K, in the temperature of transition of thorite-to-huttonite at ambient pressures could be attributed to the sluggish kinetics of the phase transition. The reason that the transition is sluggish is that the ThO_8 polyhedra in thorite become ThO_9 polyhedra in huttonite (Finch and Hanchar 2003). This sluggish behavior was observed in the calorimetry work by Mazeina et al., where only a fraction of the thorite was converted to huttonite even at 1773 K; in fact, the authors needed to heat the thorite twice in the DSC to produce pure huttonite (Mazeina et al. 2005). Furthermore, from the new phase boundary equation, we evaluate the thermochemical data of thorite and huttonite with implications of their natural formation and abundance. By using the Clapeyron equation $\frac{dP}{dT} = \frac{\Delta\Delta H}{T\Delta V}$, with its value from the boundary equation, and ΔV from the change in volume from thorite to huttonite at pressures (volumetric data in Tables S2 and S3), we can estimate the enthalpy of transition ($\Delta\Delta H$) at room temperature to be 7.0 ± 1.8 kJ/mol. With the enthalpy of formation of thorite from oxides ($\Delta H_{f,ox}$ = -6.4 ± 5.7 kJ/mol) measured by high temperature oxide melt calorimetry (Guo et al. 2016), $\Delta H_{f,ox}$ of huttonite can be derived to be 0.6 ± 6.0 kJ/mol.

Implications:

Huttonite occurs rarely in nature. The new *P*-*T* phase diagram for $ThSiO_4$ proposed in this work offers a potential thermodynamic explanation for the rarity of natural huttonite, as the stability fields of thorite and huttonite can be constrained by the updated boundary: $P(T) = (7.8 \pm 0.9\ \text{GPa}) - (0.006 \pm 0.002\ \text{Gpa/K})T$. This suggests that the onset pressure of the thorite-to-huttonite transition is 6.0 ± 1.1 Gpa, and by using the Clapeyron equation, the enthalpy of formation of huttonite is estimated to be 0.6 ± 6.0 kJ/mol at standard state conditions. This close-to-zero enthalpy suggests that huttonite is only marginally stable with respect to the oxides (ThO_2 and SiO_2) at room temperature but unstable relative to thorite below 6 Gpa, and then becomes more stable above 6 Gpa. However, the transition from thorite to huttonite may be kinetically hindered, probably due to the large energetic barrier for bonding changes from ThO_8 polyhedra in thorite to ThO_9 polyhedra in huttonite. This may generally explain the rarity of huttonite in natural systems, and huttonite may serve as a diagnostic mineral in reconstructing P-T conditions of metamorphic terrains and other geological formations.

Acknowledgements:

This work was supported by the institutional funds from the Department of Chemistry at Washington State University in the early stage, and later supported by the National Science Foundation (NSF), Division of Earth Sciences, under award No. 2149848, and Division of Materials Research, under award No. 2144792. We also acknowledge the help from the Alexandra Navrotsky Institute for Experimental Thermodynamics, and the WSU-PNNL Nuclear Science and Technology Institute. Research presented in this article was supported by the Laboratory Directed Research and Development (LDRD) program of Los Alamos National Laboratory (LANL) under project number 20180007DR. LANL, an affirmative action/equal opportunity employer, is managed by Triad National Security, LLC, for the National Nuclear Security Administration of the U.S. Department of Energy under contract 89233218CNA000001. A portion of this work was performed at GeoSoilEnviroCARS (The University of Chicago, Sector 13), Advanced Photon Source (APS), Argonne National Laboratory. GeoSoilEnviroCARS is supported by the NSF – Earth Sciences (EAR – 1634415). This research used resources of the Advanced Photon Source, a U.S. Department of Energy (DOE) Office of Science User Facility operated for the DOE Office of Science by Argonne National Laboratory under Contract No. DE-AC02-06CH11357.

Dedication:

We would like to dedicate this work to Prof. Rod C. Ewing at Stanford University (also a co-author of this paper), who unfortunately passed away during the revision of this paper. Prof. Ewing was a world-leading mineralogist and materials scientist who pioneered the scientific field of nuclear waste disposal such as using zircon-type minerals to immobilize actinides. He inspired us to pursue in-depth understanding of the structures and thermodynamics of actinide orthosilicates, including thorite and huttonite presented in this work, with the goal of high-fidelity prediction of their stabity relations and ultimate fate in a geological repository. We are deeply saddened by his passing and the loss of a visionary leader in the mineralogical community.

446 **Figures:**

447

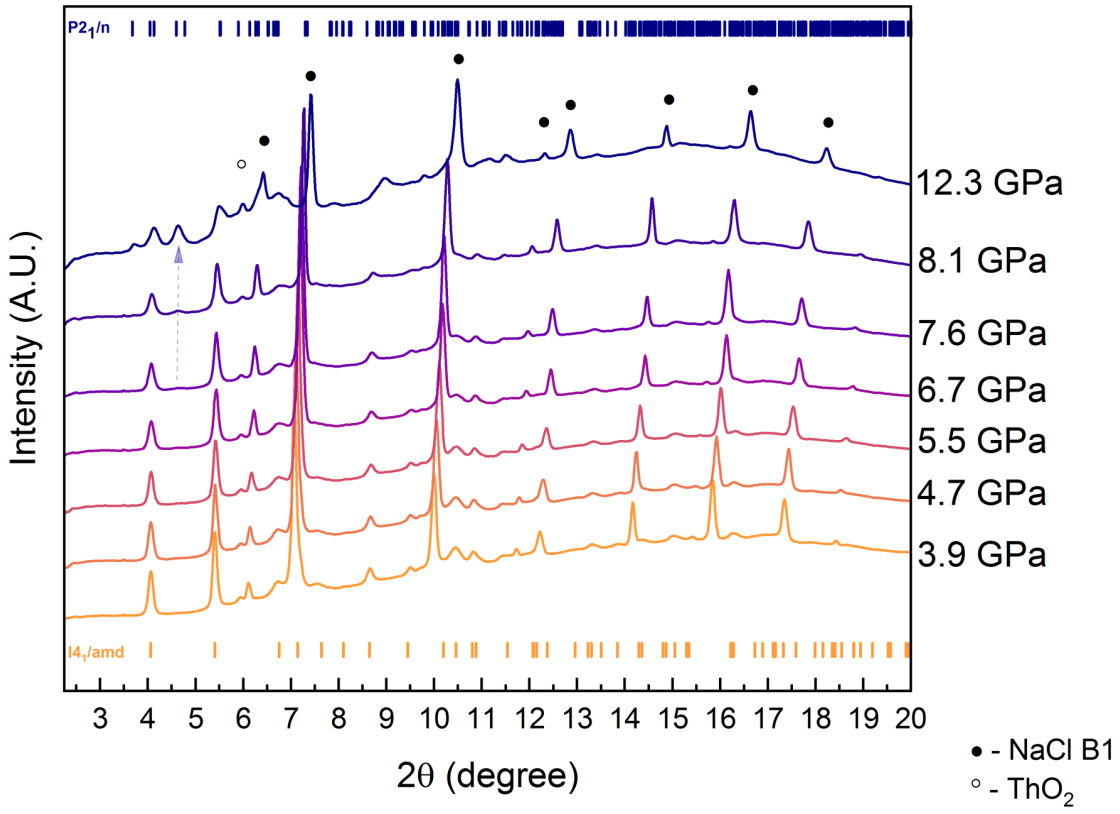

448

449 **Figure 1:** Powder XRD patterns of thorite as a function of pressure, collected using a diamond
450 anvil cell with NaCl as the pressure transmitting medium. Ticks below and above the XRD patterns
451 indicate the positions of allowed diffraction maxima for thorite and huttonite, respectively. The
452 dashed arrow around 4.608° indicates the growth of the diffraction peak related to huttonite.

453

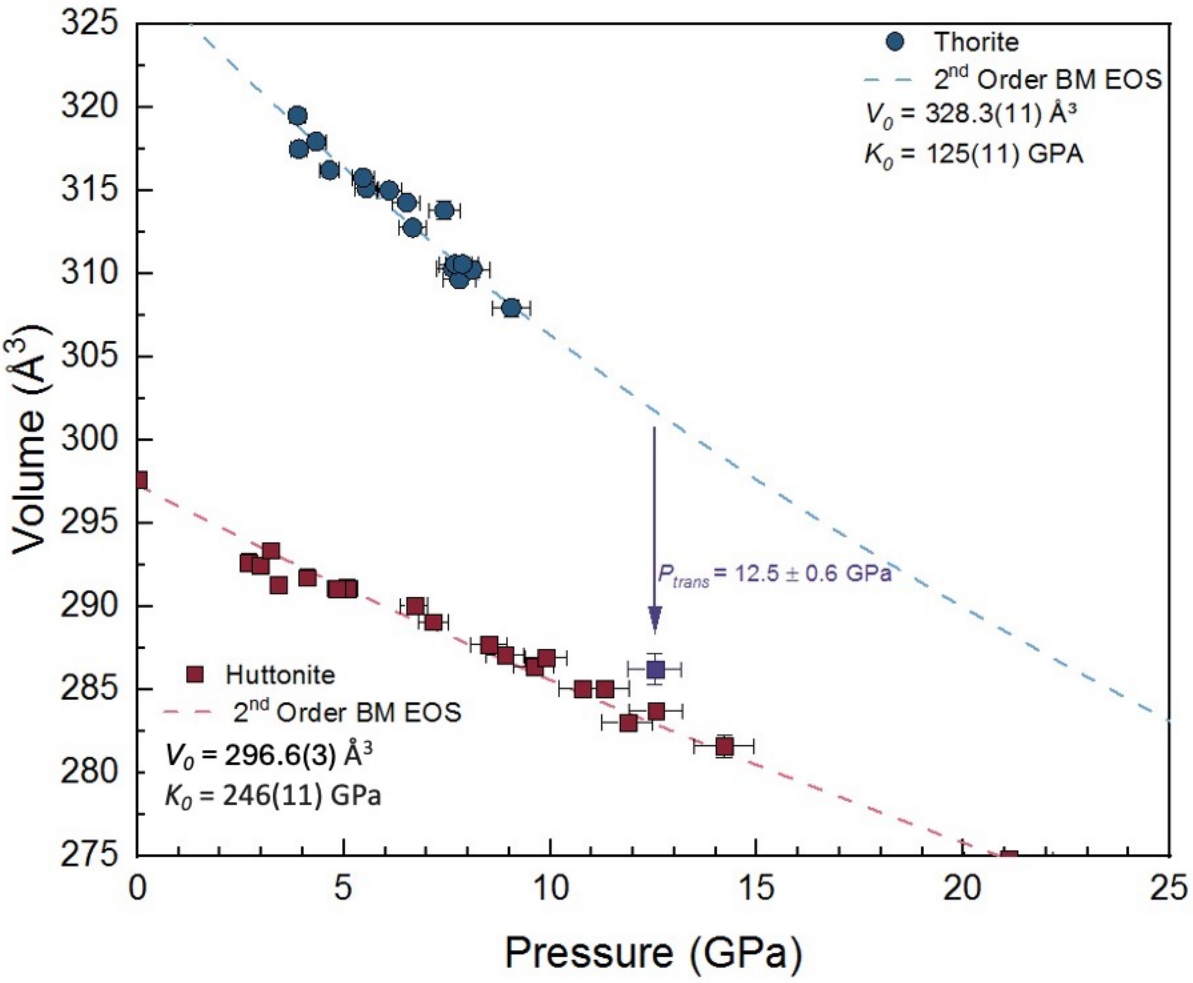

Figure 2: Variation of unit-cell volumes of $ThSiO_4$ as a function of pressure. Blue symbols represent the low-pressure thorite structured phase ($I4_1/amd$); red symbols represent the high-pressure huttonite structured phase ($P2_1/n$); and purple symbol represents $ThSiO_4$ that underwent the thorite to huttonite transition. Unit-cell volumes were determined from XRD data collected using a diamond anvil cell with NaCl as the pressure transmitting medium.

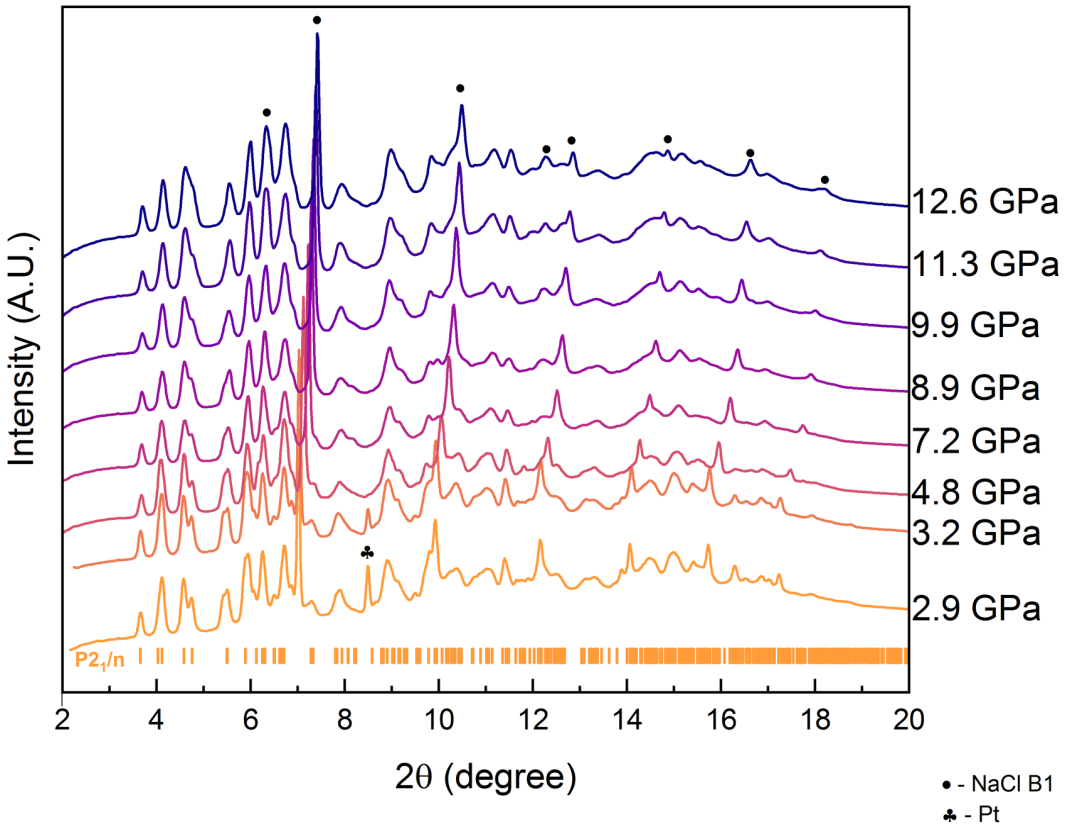

461

462 **Figure 3:** Powder XRD patterns of huttonite as a function of pressure, collected using a diamond
463 anvil cell with NaCl as the pressure transmitting medium. Ticks below indicate the positions of
464 allowed diffraction maxima for huttonite.

465

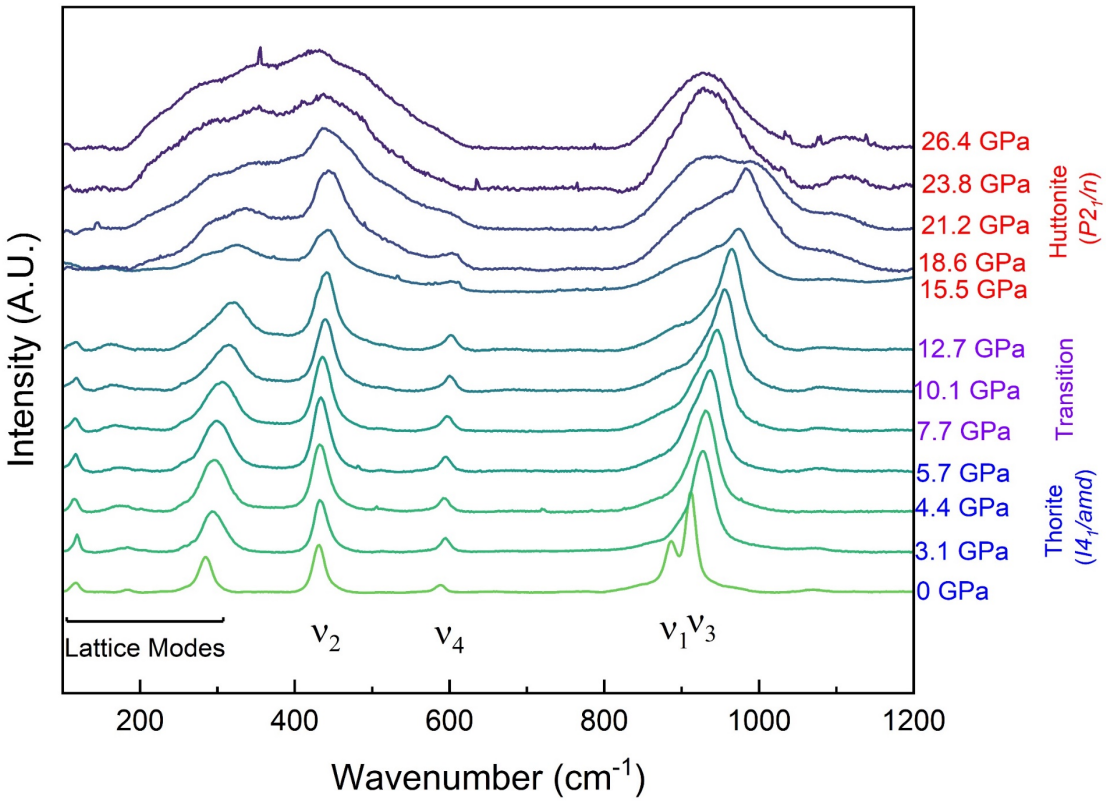

466

467 **Figure 4:** Raman spectra of $ThSiO_4$ at high pressures up to 26.4 ± 1.3 GPa.

468

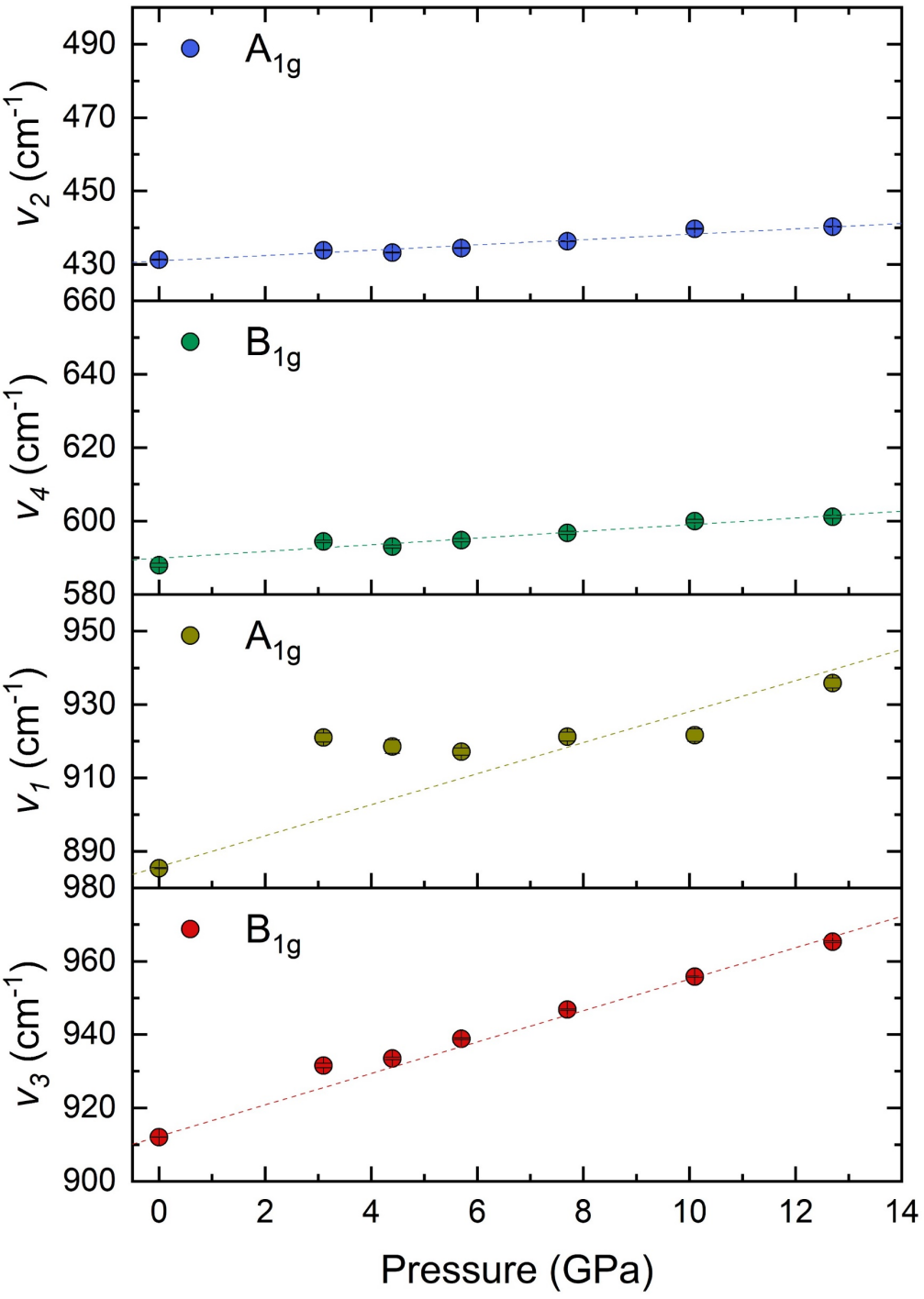

469

470 **Figure 5:** Pressure dependence of the silicate internal Raman modes of thorite up to 12.7 ± 0.6

471 GPa.

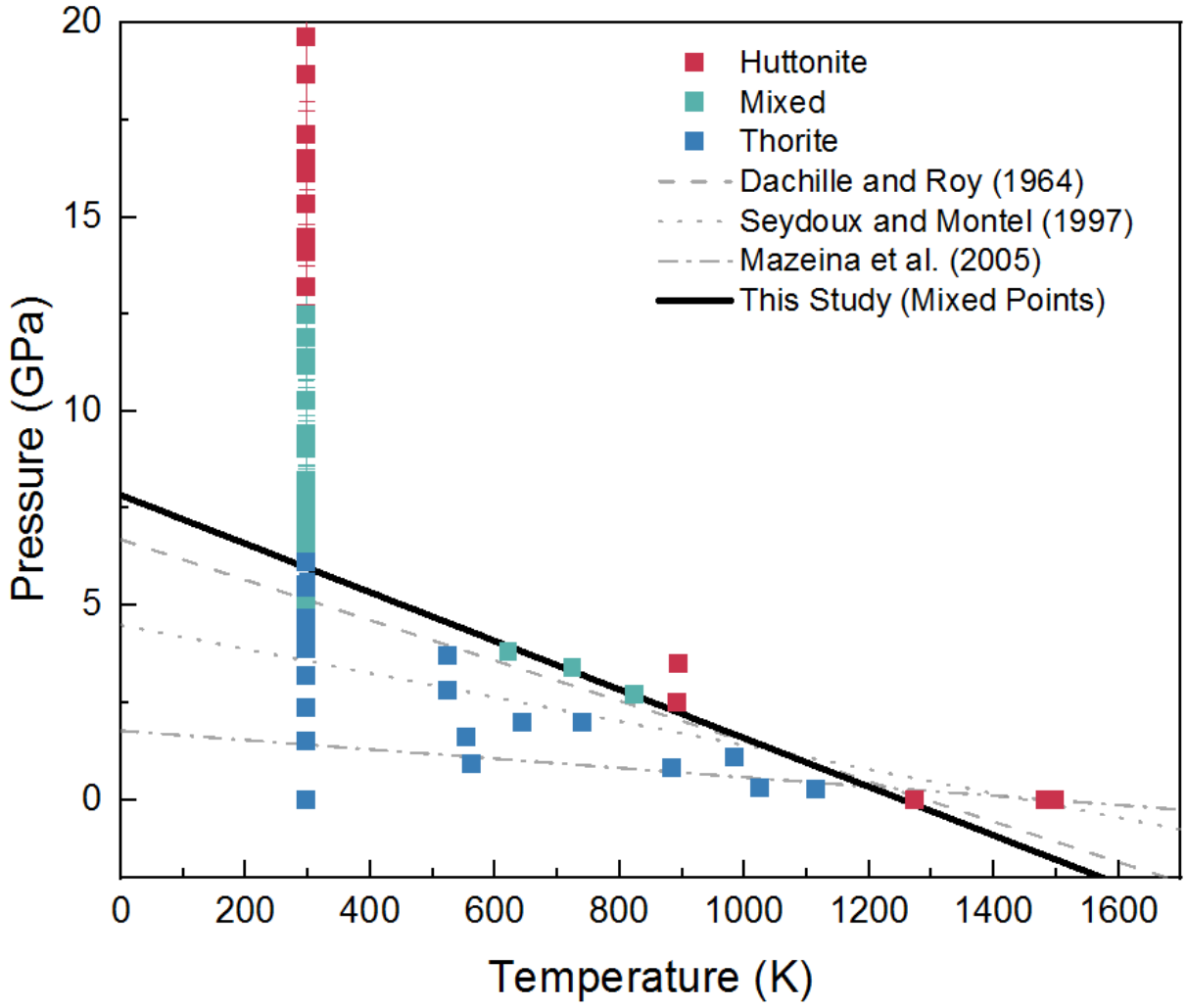

Figure 6: P–T phase diagram of $ThSiO_4$. Red squares represent huttonite, green squares represent a mixture of thorite and huttonite, and blue represent thorite. The lines represent the P-T phase boundary between thorite and huttonite. The data used in this figure were taken from Dachille and Roy (1964), Seydoux and Montel (1997), Mazeina et al. (2005), and this study.

Tables:

Table 1. Frequencies of the internal vibrational modes of SiO_4 tetrahedra of thorite in cm^{-1} and comparison with those of some other zircon structure-type orthosilicates at ambient pressure.

	v_1 (A_{1g})	v_2 (A_{1g})	v_3 (B_{2g})	v_4 (B_{2g})	*Reference*
$ThSiO_4$	885	431	912	588	This Work
$ThSiO_4$	894	439	920	593	(Syme et al. 1977)
$ThSiO_4$	887	438	914	592	(Clavier et al. 2014)
$ThSiO_4$	892	439	918	596	(Estevenon et al. 2018)
$USiO_4$	904	428	930	N.O.	(Geisler et al. 2006)
$USiO_4$	906	424	919	591	(Clavier et al. 2014)
$USiO_4$	903	424	918	592	(Strzelecki et al. 2021)
$CeSiO_4$	902	417	920	594	(Strzelecki et al. 2023)
$CeSiO_4$	903	431	919	592	(Estevenon et al. 2019a)
$CeSiO_4$	902	431	919	592	(Estevenon et al. 2019b)
$CeSiO_4$	902	416	918	593	(Strzelecki et al. 2021)
$ZrSiO_4$	974	439	1008	608	(Dawson et al. 1971)
$HfSiO_4$	984	448	1018	620	(Hoskin and Rodgers 1996)
$HfSiO_4$	979	451	1015	627	(Estevenon et al. 2020)

Table 2. Pressure derivatives ($d\nu/dP$) of the vibrational modes and Grüneisen parameters (γ_i) of $ThSiO_4$ below 12.7 GPa and comparison with the values of some other isostructural orthosilicates.

	$d\nu_1/dP$ (cm^{-1}/GPa)	$d\nu_2/dP$ (cm^{-1}/GPa)	$d\nu_3/dP$ (cm^{-1}/GPa)	$d\nu_4/dP$ (cm^{-1}/GPa)	Method	Reference
$ThSiO_4$	4.2	0.7	4.3	0.9	Experimental	This Study
$USiO_4$	5.2	1.4	6.0	3.2	Experimental	(Bauer et al. 2014)
$USiO_4$	5.6	1.2	5.4	1.8	DFT	(Bauer et al. 2014)
$CeSiO_4$	4.9	1.2	4.8	N/A	Experimental	(Strzelecki et al. 2023)
$HfSiO_4$	4.1	1.1	4.6	N/A	Experimental	(Manoun et al. 2006)
$ZrSiO_4$	4.1	1.1	4.8	N/A	Experimental	(Knittle and Williams 1993)
	γ_1	γ_2	γ_3	γ_4	Method	Reference
$ThSiO_4$	0.60	0.21	0.59	0.19	Experimental	
$USiO_4$	1.03	0.61	1.18	0.99	Experimental	(Bauer et al. 2014)
$USiO_4$	1.12	0.54	1.07	0.57	DFT	(Bauer et al. 2014)
$CeSiO_4$	0.95	0.50	0.90	N/A	Experimental	(Strzelecki et al. 2023)
$ZrSiO_4$	1.0	0.57	1.1	N/A	Experimental	(Knittle and Williams 1993)
$USiO_4$	1.03	0.61	1.18	0.99	Experimental	(Bauer et al. 2014)
$USiO_4$	1.12	0.54	1.07	0.57	DFT	(Bauer et al. 2014)

Table 3. Bulk moduli of thorite, other isostructural orthosilicates and huttonite.

Phase	**V_0 ($Å^3$)**	**K_0 (GPa)**	**PTM**	**Reference**
thorite ($ThSiO_4$)	320.7(4)	153(14)	4:1 methanol:ethanol	This study
thorite ($ThSiO_4$)	328.3(11)	125(11)	NaCl	This study
thorite ($ThSiO_4$)	324.5(6)	139(9)	averaged	This study
coffinite ($USiO_4$)	306.2(4)	188(4)	16:3:1 methanol:ethanol:water	(Zhang et al. 2009b)
coffinite ($USiO_4$)	305.58(2)	181(5)	Ne	(Bauer et al. 2014)
stetindite $CeSiO_4$)	300.8(3)	171(5)	Ne	(Strzelecki et al. 2023)
huttonite ($ThSiO_4$)	296.6(3)	246(11)	NaCl	This Study

References:

Baker, J.L., Wang, G., Ulrich, T., White, J.T., Batista, E.R., Yang, P., Roback, R.C., Park, C., and Xu, H. (2020) High-pressure structural behavior and elastic properties of U3Si5: A combined synchrotron XRD and DFT study. Journal of Nuclear Materials, 540, 152373.

Bauer, J.D., Labs, S., Weiss, S., Bayarjargal, L., Morgenroth, W., Milman, V., Perlov, A., Curtius, H., Bosbach, D., Zänker, H., and others (2014) High-pressure phase transition of coffinite, USiO 4. Journal of Physical Chemistry C, 118, 25141–25149.

Birch, F. (1978) Finite strain isotherm and velocities for single-crystal and polycrystalline NaCl at high pressures and 300°K. Journal of Geophysical Research, 83, 1257.

Bose, P.P., Mittal, R., and Chaplot, S.L. (2009) Lattice dynamics and high pressure phase stability of zircon structured natural silicates. Physical Review B - Condensed Matter and Materials Physics, 79, 1–8.

Clavier, N., Szenknect, S., Costin, D.T., Mesbah, A., Ravaux, J., Poinssot, C., and Dacheux, N. (2013) Purification of uranothorite solid solutions from polyphase systems. Journal of Nuclear Materials, 441, 73–83.

Clavier, N., Szenknect, S., Costin, D.T., Mesbah, A., Poinssot, C., and Dacheux, N. (2014) From thorite to coffinite: A spectroscopic study of Th1-xUxSiO4 solid solutions. Spectrochimica Acta - Part A: Molecular and Biomolecular Spectroscopy, 118, 302–307.

Dacheux, N., Brandel, V., Genet, M., Bak, K., and Berthier, C. (1996) Solid solutions of uranium and thorium phosphates: synthesis, characterization and X-ray photoelectron spectroscopy. New Journal of Chemistry, 20, 301–310.

Dachille, F., and Roy, R. (1964) Effectiveness of shearing stresses in accelerating solid-phase reactions at low temperatures and high pressures. Journal of Geology, 72, 243–247.

Dawson, P., Hargreave, M.M., and Wilkinson, G.R. (1971) The vibrational spectrum of zircon (ZrSiO4). Journal of Physics C: Solid State Physics, 4, 240–256.

Dewaele, A., Belonoshko, A.B., Garbarino, G., Occelli, F., Bouvier, P., Hanfland, M., and Mezouar, M. (2012) High-pressure-high-temperature equation of state of KCl and KBr. Physical Review B - Condensed Matter and Materials Physics, 85, 1–7.

Ehlers, A.M., Zaffiro, G., Angel, R.J., Boffa-Ballaran, T., Carpenter, M.A., Alvaro, M., and Ross, N.L. (2022) Thermoelastic properties of zircon: Implications for geothermobarometry. American Mineralogist, 107, 74–81.

524 Estevenon, P., Welcomme, E., Szenknect, S., Mesbah, A., Moisy, P., Poinssot, C., and Dacheux,
525 N. (2018) Multiparametric Study of the Synthesis of ThSiO4 under Hydrothermal Conditions.
526 Inorganic Chemistry, 57, 9393–9402.
527 Estevenon, P., Welcomme, E., Szenknect, S., Mesbah, A., Moisy, P., Poinssot, C., and Dacheux,
528 N. (2019a) Preparation of CeSiO4 from aqueous precursors under soft hydrothermal
529 conditions . Dalton Transactions, 48, 7551–7559.
530 Estevenon, P., Kaczmarek, T., Vadot, F., Dumas, T., Solari, P.L., Welcomme, E., Szenknect, S.,
531 Mesbah, A., Moisy, P., Poinssot, C., and others (2019b) Formation of CeSiO4 from cerium
532 (III) silicate precursors. Dalton Transactions, 48, 10455–10463.
533 Estevenon, P., Kaczmarek, T., Rafiuddin, M.R., Welcomme, E., Szenknect, S., Mesbah, A.,
534 Moisy, P., Poinssot, C., and Dacheux, N. (2020) Soft hydrothermal synthesis of Hafnon,
535 HfSiO4. Crystal Growth Design, 20, 1820–1828.
536 Farnan, I., Balan, E., Pickard, C.J., and Mauri, F. (2003) The effects of radiation on local structure
537 in the crystalline fraction of ZrSiO4: Investigating the 29Si NMR response to pressure in
538 zircon and reidite. American Mineralogist, 88, 1663–1667.
539 Finch, C.B., Harris, L.A., and Clark, G.W. (1964) The thorite → huttonite phase transformation
540 as determined by growth of synthetic thorite and huttonite single crystals. American
541 Mineralogist, 49, 782–785.
542 Finch, R.J., and Hanchar, J.M. (2003) Structure and chemistry of zircon and zircon-group minerals.
543 In J.M. Hanchar and P.W.O. Hoskin, Eds., Reviews in Mineralogy and Geochemistry: Zircon
544 Vol. 53, pp. 1–26. Mineralogical Society of America.
545 Frondel, C. (1958) Systematic Mineralogy of Uranium and Thorium, 11–18 p. U. S. Geological
546 Survey Bulletin Vol. 1064.
547 Fuchs, L.H., and Hoekstra, H.R. (1959) The Preparation and Properties of Uranium (IV) Silicate.
548 The American Mineralogist, 44, 1057–1063.
549 Geisler, T., Burakov, B.E., Zirlin, V., Nikolaeva, L., and Pöml, P. (2006) A Raman spectroscopic
550 study of high-uranium zircon from the Chernobyl “lava.” European Journal of Mineralogy,
551 17, 883–894.
552 Gonzalez-Platas, J., Alvaro, M., Nestola, F., and Angel, R. (2016) EosFit7-GUI: A new graphical
553 user interface for equation of state calculations, analyses and teaching. Journal of Applied
554 Crystallography, 49, 1377–1382.

555 Gucsik, A., Zhang, M., Koeberl, C., Salje, E.K.H., Redfern, S.A.T., and Pruneda, J.M. (2004)
556 Infrared and Raman spectra of ZrSiO 4 experimentally shocked at high pressures .
557 Mineralogical Magazine, 68, 801–811.
558 Guo, X., Szenknect, S., Mesbah, A., Labs, S., Clavier, N., Poinssot, C., Ushakov, S. V., Curtius,
559 H., Bosbach, D., Ewing, R.C., and others (2015) Thermodynamics of formation of coffinite,
560 USiO4. Proceedings of the National Academy of Sciences, 112, 6551–6555.
561 Guo, X., Szenknect, S., Mesbah, A., Clavier, N., Poinssot, C., Wu, D., Xu, H., Dacheux, N., Ewing,
562 R.C., and Navrotsky, A. (2016) Energetics of a uranothorite (Th1-xUxSiO4) solid solution.
563 Chemistry of Materials, 28, 7117–7124.
564 Guo, X., Lü, X., White, J.T., Benmore, C.J., Nelson, A.T., Roback, R.C., and Xu, H. (2019) Bulk
565 moduli and high pressure crystal structure of U_3Si_2. Journal of Nuclear Materials, 523, 135–
566 142.
567 Hazen, R.M., and Finger, L.M. (1979) Crystal structure and compressibility of zircon at high
568 pressure. American Mineralogist, 64, 196–201.
569 Hoekstra, H.R., and Fuchs, L.H. (1956) Synthesis of Coffinite - $USiO_4$. Science, 123, 105.
570 Hoskin, P.W.O., and Rodgers, K.A. (1996) Raman spectral shift in the isomorphous (Zr1-
571 xHfx)SiO4. European journal of solid state and inorganic chemistry, 33, 1111–1121.
572 Hubert, S., Heisbourg, G., Dacheux, N., and Moisy, P. (2008) Effect of Inorganic Ligands and
573 Hydrogen Peroxide on ThO2 Dissolution. Behaviour of Th0.87Pu0.13O2 during Leaching
574 Test, Inorganic Chemistry, 33, 1111–1121.
575 Jin, G.B., and Soderholm, L. (2015) Solid-state syntheses and single-crystal characterizations of
576 three tetravalent thorium and uranium silicates. Journal of Solid State Chemistry, 221, 405–
577 410.
578 Klotz, S., Chervin, J.C., Munsch, P., and Le Marchand, G. (2009) Hydrostatic limits of 11 pressure
579 transmitting media. Journal of Physics D: Applied Physics, 42.
580 Knittle, E., and Williams, Q. (1993) High-pressure Raman spectroscopy of $ZrSiO_4$: observation of
581 the zircon to scheelite transition at 300 K. American Mineralogist, 78, 245–252.
582 Kolesov, B.A., Geiger, C.A., and Armbruster, T. (2001) The dynamic properties of zircon studied
583 by single-crystal X-ray diffraction and Raman spectroscopy. European Journal of
584 Mineralogy, 13, 939–948.

585 Lü, X., Stoumpos, C.C., Hu, Q., Ma, X., Zhang, D., Guo, S., J.;, H., Bu, K., Guo, X., Wang, Y.,
586 and others (2020) Regulating off-centering distortion maximizes photoluminescence in halide
587 perovskites. National Science Review.
588 Luo, W., and Ahuja, R. (2008) High pressure structural phase transition in zircon (ZrSiO4). Journal
589 of Physics: Conference Series, 121.
590 Manoun, B., Downs, R.T., and Saxena, S.K. (2006) A high-pressure Raman spectroscopic study
591 of hafnon, HfSiO4. American Mineralogist, 91, 1888–1892.
592 Mao, H.K., Xu, J., and Bell, P.M. (1986) Calibration of the ruby pressure gauge to 800 kbar under
593 quasi-hydrostatic conditions. Journal of Geophysical Research, 91, 4673–4676.
594 Marcial, J., Zhang, Y., Zhao, X., Xu, H., Mesbah, A., Nienhuis, E.T., Szenknect, S., Lin, J., Qi,
595 L., Migdissov, A., and others (2021) Thermodynamic non-ideality and disorder heterogeneity
596 in actinide silicate solid solutions. Materials Degradation, 5, 1–14.
597 Mazeina, L., Ushakov, S. V., Navrotsky, A., and Boatner, L.A. (2005) Formation enthalpy of
598 ThSiO4 and enthalpy of the thorite → huttonite phase transition. Geochimica et
599 Cosmochimica Acta, 69, 4675–4683.
600 Mesbah, A., Szenknect, S., Clavier, N., Lozano-Rodriguez, J., Poinssot, C., Den Auwer, C.,
601 Ewing, R.C., and Dacheux, N. (2015) Coffinite, USiO4, Is Abundant in Nature: So Why Is It
602 so Difficult to Synthesize? Inorganic Chemistry, 54, 6687–6696.
603 Mondal, S.K., Das, P.K., Mandal, N., and Arya, A. (2020) A novel approach to the structural
604 distortions of U/Th snub-disphenoids and their control on zircon → reidite type phase
605 transitions of U1-xThxSiO4. Journal of Physics Condensed Matter, 32.
606 Nasdala, L., Zhang, M., Kempe, U., Panczer, G., Gaft, M., Andrut, M., and Plötze, M. (2003)
607 Spectroscopic methods applied to zircon. In J.M. Hanchar and P.W.O. Hoskin, Eds., Reviews
608 in Mineralogy and Geochemistry: Zircon pp. 427–467. Mineralogical Society of America.
609 Navrotsky, A., Shvareva, T., and Guo, X. (2013) Thermodynamics of Uranium Minerals and
610 Related Materials. In P.C. Burns and G.E. Sigmon, Eds., Mineralogical Association of
611 Canada Short Course 43 pp. 147–164. Mineralogical Association of Canada, Winnipeg.
612 Ono, S., Tange, Y., Katayama, I., and Kikegawa, T. (2004a) Equation of State of ZrSiO4 phases
613 in the upper mantle. American Mineralogist, 89, 185–188.
614 Ono, S., Funakoshi, K., Nakajima, Y., Tange, Y., and Katsura, T. (2004b) Phase transition of
615 zircon at high P-T conditions. Contributions to Mineralogy and Petrology, 147, 505–509.

Pabst, A., and Hutton, C.O. (1951) Huttonite, a new monoclinic thorium silicate. Am. Mineral., 36, 60–69.

Prescher, C., and Prakapenka, V.B. (2015) DIOPTAS: A program for reduction of two-dimensional X-ray diffraction data and data exploration. High Pressure Research, 35, 223–230.

Reid, A.F., and Ringwood, A.E. (1969) Newly Observed High Pressure Transformation in Mn3O4, CaAl2O4, and ZrSiO4. Earth and Planetary Science Letters, 6, 205–208.

Seydoux, A.M., and Montel, J.M. (1997) Experimental determination of the thorite-huttonite phase transition. EUG IX, Terra Nova 9, Abstract Supplement, 1.

Shannon, R.D. (1976) Revised Effective Ionic Radii and Systematic Studies of Interatomic Distances in Halides and Chalcogenides. Acta Crystallographica Section A, 32, 751–766.

Stangarone, C., Angel, R.J., Prencipe, M., Mihailova, B., and Alvaro, M. (2019) New insights into the zircon-reidite phase transition. American Mineralogist, 104, 830–837.

Strzelecki, A.C., Bourgeois, C., Kriegsman, K.W., Estevenon, P., Wei, N., Szenknect, S., Mesbah, A., Wu, D., Ewing, R.C., Dacheux, N., and others (2020) Thermodynamics of $CeSiO_4$: Implications for Actinide Orthosilicates. Inorganic Chemistry, 59, 13174–13183.

Strzelecki, A.C., Barral, T., Estevenon, P., Mesbah, A., Goncharov, V., Baker, J., Bai, J., Clavier, N., Szenknect, S., Migdissov, A., and others (2021) The Role of Water and Hydroxyl Groups in the Structures of Stetindite and Coffinite, MSiO4 (M = Ce, U). Inorganic Chemistry.

Strzelecki, A.C., Ren, Y., Chong, S., Riley, B.J., Xu, H., McCloy, J.S., and Guo, X. (2022a) Structure and thermodynamics of calcium rare earth silicate oxyapatites, Ca2RE8(SiO4)6O2 (RE = Pr, Tb, Ho, Tm). Physics and Chemistry of Minerals, 49, 13.

Strzelecki, A.C., Reece, M.E., Zhao, X., Yu, W., Benmore, C.J., Ren, Y., Alcorn, C.D., Migdisov, A., Xu, H., and Guo, X. (2022b) Thermodynamics of mixing HREE in Xenotime Solid Solution (Er(x)Yb(1-x)PO4). ACS Earth and Space Chemistry.

Strzelecki, A.C., Zhao, X., Baker, J.L., Estevenon, P., Barral, T., Mesbah, A., Popov, D., Chariton, S., Prakapenka, V., Ahmed, S., and others (2023) High-Pressure Structural and Thermodynamic Properties of Cerium Orthosilicates ($CeSiO_4$). The Journal of Physical Chemistry C, 127, 4225–4238.

Strzelecki, A.C., Zhao, X., Estevenon, P., Xu, H., Dacheux, N., Ewing, R.C., and Guo, X. (2024) Crystal chemistry and thermodynamic properties of zircon structure-type materials. American Mineralogist, 109, 225–242.

Syme, R.W.G., Lockwood, D.J., and Kerr, H.J. (1977) Raman spectrum of synthetic zircon ($ZrSiO_4$) and thorite. Solid State Phys., 10, 1335–1348.

Tange, Y., and Takahashi, E. (2004) Stability of the high-pressure polymorph of zircon (ZrSiO4) in the deep mantle. Physics of the Earth and Planetary Interiors, 143, 223–229.

Taylor, M., and Ewing, R.C. (1978) The crystal structures of the $ThSiO_4$ polymorphs: huttonite and thorite. Acta Crystallographica Section B Structural Crystallography and Crystal Chemistry, 34, 1074–1079.

Toby, B.H., and Von Dreele, R.B. (2013) GSAS-II: The genesis of a modern open-source all purpose crystallography software package. Journal of Applied Crystallography, 46, 544–549.

White, W.M. (2015) Isotope Geochemistry, 1st ed., 72–100 p. John Wiley & Sons.

Winter, J.D. (2013) Principles of Igneous and Metamorphic Petrology, 2nd ed., 166–190 p. Pearson.

Xu, H., Zhao, Y., Zhang, J., Wang, Y., Hickmott, D.D., Daemen, L.L., Hartl, M.A., and Wang, L. (2009) Anisotropic elasticity of jarosite: A high-P synchrotron XRD study. American Mineralogist, 95, 19–23.

Xu, H., Guo, X., and Bai, J. (2017) Thermal behavior of polyhalite: a high-temperature synchrotron XRD study. Physics and Chemistry of Minerals, 44, 125–135.

Zha, C.S., Mibe, K., Bassett, W.A., Tschauner, O., Mao, H.K., and Hemley, R.J. (2008) P-V-T equation of state of platinum to 80 GPa and 1900 K from internal resistive heating/x-ray diffraction measurements. Journal of Applied Physics, 103.

Zhang, F.X., Pointeau, V., Shuller, L.C., Reaman, D.M., Lang, M., Liu, Z., Hu, J., Panero, W.R., Becker, U., Poinssot, C., and others (2009a) Structural transitions and electron transfer in coffinite, USiO 4, at high pressure. American Mineralogist, 94, 916–920.

——— (2009b) Structural transitions and electron transfer in coffinite, USiO 4, at high pressure. American Mineralogist, 94, 916–920.

Zhang, J., Celestian, A., Parise, J.B., Xu, H., and Heaney, P.J. (2002) A new polymorph of eucryptite (LiAlSiO4), ε-eucryptite, and thermal expansion of α- and ε-eucryptite at high pressure. American Mineralogist2, 87, 556–571.

Zhao, X., Strzelecki, A., Dacheux, N., Qi, L., and Guo, X. (2024) Phonon Softening Induced Phase Transition of $CeSiO_4$: A Density Functional Theory Study. Dalton Transactions.